Published on

ACS applied materials & interfaces, vol. 10, issue 9, 2018, 8132–8140

Publication Date: February 7, 2018

DOI: https://doi.org/10.1021/acsami.7b16068

DOI: 10.1002/ ((please add manuscript number))
Article type: Full paper

Oxygen impurities link bistability and magnetoresistance in organic spin valves.

Ilaria Bergenti, Francesco Borgatti, Marco Calbucci, Alberto Riminucci, Raimondo Cecchini, Patrizio Graziosi, Donald MacLaren, Angelo Giglia, Jean Pascal Rueff, Denis Céolin, Luca Pasquali, Valentin Dediu*

I. Bergenti, F. Borgatti, A. Riminucci, P. Graziosi, V. Dediu
CNR-ISMN, via Gobetti 101, 40129 Bologna, Italy
E-mail: ilaria.bergenti@cnr.it

M. Calbucci
Institute of Molecular Science (ICMol) Catedrático José Beltrán Martínez 2 46980 Paterna Spain

R. Cecchini
MDM Laboratory, IMM-CNR, Via C. Olivetti 2, 20864 Agrate Brianza, MB, Italy

DA. MacLaren
SUPA, School of Physics and Astronomy, University of Glasgow, Glasgow G12 8QQ

A. Giglia
IOM-CNR, s.s. 14, Km. 163.5 in AREA Science Park, Basovizza, 34149 Trieste, Italy

J. -P. Rueff, D. Céolin
Synchrotron SOLEIL, Saint-Aubin, BP 48,F-91192 Gif-sur-Yvette Cedex, France

L. Pasquali
Dipartimento di Ingegneria E. Ferrari, Via Vivarelli 10, 41125 Modena, Italy
IOM-CNR, s.s. 14, Km. 163.5 in AREA Science Park, Basovizza, 34149 Trieste, Italy
Department of Physics, University of Johannesburg, P.O. Box 524, Auckland Park 2006, South Africa

Keywords: organic spintronics, spin valve, spin transport, impurity levels, oxygen dopants

Abstract

Vertical cross-bar devices based on manganite and cobalt injecting electrodes and metal-quinoline molecular transport layer are known to manifest both magnetoresistance and electrical bistability. The two effects are strongly interwoven, inspiring new device applications such as electrical control of the magnetoresistance and magnetic modulation of bistability. By non destructive in operando X-ray Spectroscopy, we show direct evidences of the involvement

of the molecular material in the mechanism of bistability in LSMO/Gaq_3/AlO_x/Co devices. In addition to this, a significant fraction of oxygen ions migrates under voltage polarity, resulting in a modification of the electronic properties of the organic material and of the oxidation of the AlOx tunnel barrier. Conductivity switching is then associated to variable oxygen doping of the Gaq_3. Linking finally the bistability and spintronic properties, the effects of oxygen doping of the molecular transport layer represent the first experimental evidence in favor of the proposed recently impurity band model describing the GMR in similar devices.

1. Introduction

Resistive switching (RS) behavior in organic devices has excited substantial attention because, in addition to the well-known aspects of high performance and low volatility that are inherent to RS memory, the use of organic components would yield easy-to-process, flexible devices.[1] RS has been reported for a wide variety of organic semiconductors including metal quinoline complexes.[2] Typical device configurations are simple and consist of two metallic electrodes sandwiching a semiconducting organic layer; their current–voltage (IV) characteristics are dependent on a pre-applied “writing” voltage pulse or on voltage-sweep directions and, in most cases, it is not volatile, i.e it persists when power is turned off [1]. Recent experiments [3] indicate that when the metallic electrodes are ferromagnetic (FM), magnetoresistance (MR) may also occur[4]. In our previous papers [3a, 3b], we clearly demonstrated that MR can be turned “on” and “off” as well as smoothly tuned between a number of non-volatile states depending on the device resistive state obtaining a full electrical control of MR. This ‘multifunctionality’ correlating electric and spin phenomena is tantalizing for the development of new devices[5], with potential applications in multibit nonvolatile data storage and neuromorphic computing[5b, 6].

In spite of significant achievements obtained recently in spintronics including molecular materials, from very high magnetoresistance values[7] to wise MR reproducibility mainly in case of devices involving manganite and cobalt spin polarised injectors and metal-quinoline transport layers[8], a comprehensive theory describing both the spin transport and the rise of magnetoresistance is basically missing [9] . Spin transport was first interpreted by extending the so call “conductivity mismatch” to organic semiconductors [10] involving injection in HOMO-LUMO levels, later a multistep tunneling was considered in case ultra thin organic layer [11] to account for the peculiar voltage dependence and for the absence of Hanle effects[12]. More recently, magnetoresistance features were explained by spin-dependent electron tunnelling into the impurity broad band located in the gap between molecular orbitals [13]. In such complex scenario for the interpretation of spin effects, the correlation of electrical bistability and magnetoresistance has obviously risen expectations for an additional way of inspecting the transport behavior, both for spin and charge properties

Concerning bistability, hysteretic IV behavior has been observed in a large number of organic materials from polymers to small molecule and are explained either by charging related phenomena or by filament formation related phenomena[1, 14]. The former hypothesis is associated to charge-transfer processes in donor-acceptor systems and involves the presence of metallic clusters embedded in the organic layer[15], the latter is explained by the formation of locally highly conductive channels (filaments) and refers to redox effects[16].

Two hypothesis have been considered in literature for the correlation of the bistability and magnetoresistance, none of them proven experimentally. For the first case MR originates from spin-dependent electron tunneling into highly conductive filamentary paths[17]. Alternatively, a tunnel barrier has been suggested to arise [3c] at the FM/organic interface, with the barrier being reversibly modified during RS cycles by redox mechanism, thereby modifying the magnetic injection and producing MR.

In this paper, by combining spectroscopic investigations and electrical characterization, we identify that voltage bias application determines oxygen migration within the organic spacer and the reversible modification of the molecule electronic configuration. Experimental evidences link univocally the variable oxygen doping of the organic molecule to impurity driven conductivity effects. In turn, MR signal is a results of spin transport in the organic layer across oxygen impurity states. Our investigation provides a key element for the development of comprehensive picture of spin effects in organics.

2. Results and discussion

Cross bar devices were fabricated with an area of $1mm^2$ and consisted of an ultra thin (10 to 15 nm) Gaq_3 [tris-(8-hydroxyquinoline) Gallium] layer sandwiched between a 20-nm-thick $La_{0.7}Sr_{0.3}MnO_3$ (LSMO) film grown on a $SrTiO_3$ (100) substrate, and a 7-nm-thick Co top electrode (inset of **Figure1**). An AlO_x tunnel barrier was deposited between the Gaq_3 and Co layers to minimize the penetration of Co atoms into the organic layer[18]. Gaq_3 was considered instead of the well known Alq_3 [19] because it provides similar magnetoelectric behavior, but it allows to decouple the spectroscopic signal originating from the AlO_x barrier and from the organic layer. **Figure 1a** shows the typical hysteretic behavior of the current-voltage characteristic, which depends on the polarity of the applied voltage[3b] (with respect to the grounded Co top electrode). Initially, devices are in a low resistance state (R_{IRS}(0.1V)~ 25 KΩ) that we call IRS; the I-V characteristic is marked as (1). From the IRS, the device can be set to a high resistance state (HRS) by the application of a sufficiently negative voltage. In figure 1a the device in the HRS reaches higher R_{HRS}~1MΩ at 0.1 V and is marked as (2). This state is non-volatile and in order to set the device to a low-resistance-state (LRS marked as (3) with R_{LRS}(0.1V) ~4 kΩ at 0.1 V) we must apply a sufficiently positive voltage. In analogy with what was observed in other organic bistable devices [20], our spin valves do not require an electro-

forming pulse to enable the bistability. In comparison, electro-forming is commonly required in oxide-based RS devices[21] and is usually affected by the application of a high voltage. As expected[3b], a negative MR is present in the LRS (~8%) which gradually decreases by increasing the resistance of the device (**figure 1b)** eventually eliminating the MR for enough high resistance (1MΩ).

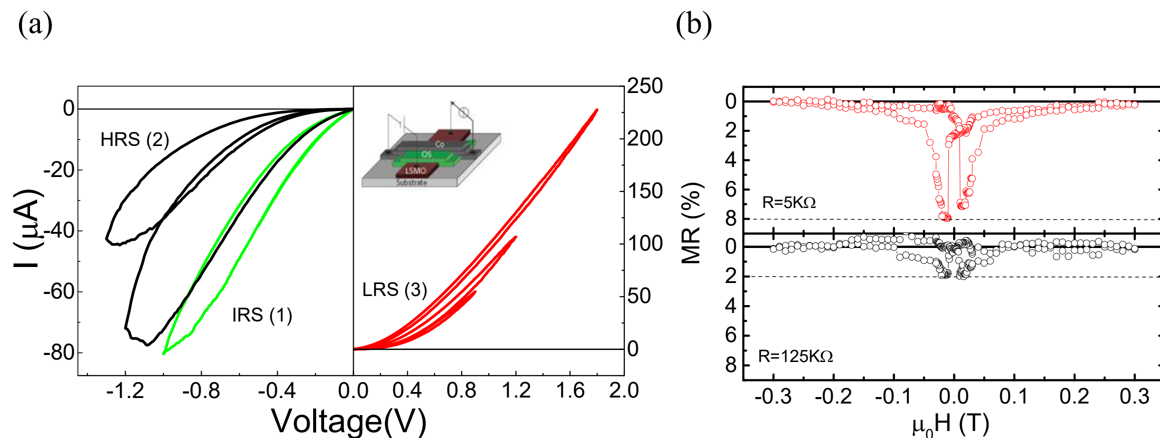

Figure 1 (a) I–V curves of LSMO/ Gaq_3/AlO_x/Co ultra thin device at RT displaying the bistability effect. Inset shows the device structure (b) Negative magnetoresistive response for two different resistive states: LRS (R=5kΩ, MR 8%) and HRS (R=125kΩ, MR 2%) measured at V_{bias}=-0.1V.

Electrical characteristics in our devices are consistent with previous investigations on similar samples [3b]. No consensus emerges from the literature on the charge conduction mechanism for such ultra thin device even if some typical signatures are found: I-V characteristic are non linear [11b] [22] [23] and device resistances have a moderate semiconductive behavior [24]. In few cases the thickness dependence of resistivity has been demonstrated [11b] indicating multi step tunneling mechanism as the most probable in such thickness regimes that nominally involves n=10 molecules.

To gain insight into the difference in transport between different resistive states, we carried out impedance spectroscopy (V_{AC}=0.01V V_{DC}=-0.1V). The impedance was modeled as a parallel RC loop with a series resistance, R_S (**Figure 2a**).

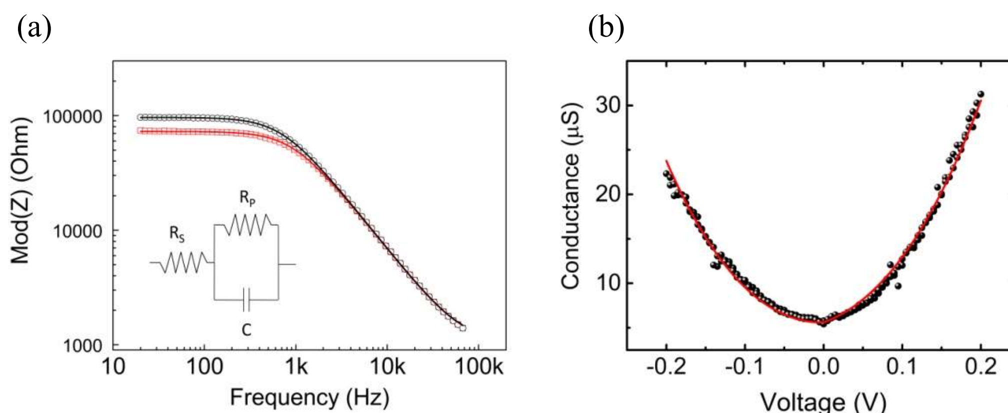

Figure 2 (a)Impedance spectra of two different resistive states. The line is the fit to the equivalent circuit of a R_PC-parallel unit in series with a resistor (R_s). (b) HRS conductance-voltage at 300K. The solid line represents fit to amorphous tunneling model.

In each impedance spectrum, the impedance magnitude showed a plateau at low frequencies and decreased above a cut off frequency. Typically, for two different resistive states an almost identical capacitance of C= 2.36 10^{-9}F was found. This value is in agreement with the geometrical value calculated using a relative permittivity of ε_r= 4 as expected for a metal quinoline layer[25], indicating that the RS was not caused by an extraneous capacitive mechanism at the electrode/organic layer interface and can therefore not be responsible for the conductivity of the individual device states. The series resistance was very low for both states (Rs ~1KΩ) and was attributed to the electrodes whilst the parallel resistance varied during the transition in different resistive states (in Fig 2 from 95kΩ to71kΩ). These results indicate that RS is dominated by the increase of the parallel resistance similarly to other organic based memory devices [26]. The charging effect model can be ruled out to play a major role in RS due to the constant C value [27] while the filamentary mechanism seems the most appropriate accounting for the different bulk conductivity of the organic materials. The microscopic origin of filaments is still debated[28] and could also rely to the specific device configuration: some experiments indicate that they are set after the migration of metallic clusters or ions from electrodes onto the organic layer[16b], others involve inhomogeneous conduction of the organic

layer itself due to doping or degradation[29]. Being the correlation between conductive properties and magnetoresistance the key element in our devices, we explore the nature of transport by the analysis of differential conductance. The differential conductance at low voltage, reported in **figure 2b**, is not constant, which excludes conduction by purely metallic filaments, in contrast to the devices described in [30]. Our data are consistent with a transport mechanism that involves localized states forming a preferential path for conductance. We find that a hopping conductance similar to that described by Xu *et al.*[31] is an effective description (see SI1). Conductance at low bias was represented by a bias-independent term, which includes the direct and resonant tunneling contributions, and a bias-dependent term to account for the onset of hopping processes. Hopping involving up to three localized states fits the experimental data well. Hopping distances of only a few nanometres are then estimated, indicating that a thinning of the layers' thickness with respect to nominal one should be expected. Possible reduction of the Co-LSMO separation has been investigated by TEM and are presented in **figure 3**. The TEM images indicate the deposition of LSMO to be of good quality, with a clear epitaxial relationship with the STO substrate. The Gaq_3 layer is amorphous, as expected, and the AlO_x layer is discernable as a uniform, thin band beneath the Co electrode, which is polycrystalline(Figure 3a). EELS signals reveal the clear laminar structure and reveal in particular the oxygen band beneath the top Co electrode that is consistent with the presence of a continuous AlO_x barrier layer (Figure 3b , 3c and SI2). Some regions of the devices, however, appeared more defective, as illustrated in figure 3d. Crystalline outgrowths were occasionally observed in the LSMO layer and are assumed to have grown during the deposition process since the encapsulating Gaq_3 and Co layers tend to be conformal. In addition, some thickness variations were observed in the Gaq_3 layer, such as that observed in the middle of figure 3d.

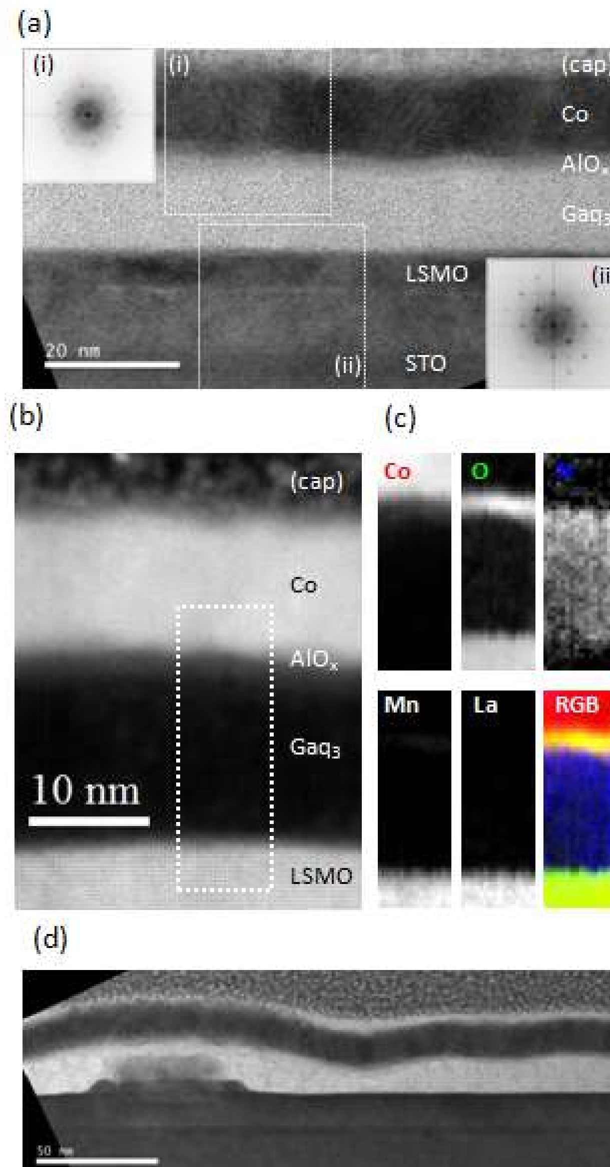

Figure 3 (a) Cross sectional TEM image of a typical device with the layer compositions indicated. Fourier transforms (inset) of the regions labeled (i) and (ii) indicate that the Co layer is polycrystalline and the LSMO and STO have a clear epitaxial relationship. (b)Electron energy loss spectroscopic analysis of a typical device: Dark field STEM image with major layers labeled. Heavier elements appear darkest and the region used for EELS analysis is indicated. (c) Composition maps showing the distribution of elements within the analysed region, each panel indicating the relative strength of background-subtracted EELS signal. The final panel is a red-green-blue composite of the Co, O and N signals. (d) Some regions of devices were found to be defective, with (left of image) mesa-like outgrowths from the LSMO apparent in addition to occasional thickness variations in the Gaq_3 layer (middle of image).

Both structural details will have the effect of reducing the separation of the two electrodes and such nano-regions are good candidates for localized conduction paths that is limited to few hops. In operando X-ray Photoelectron Spectroscopy (HAXPES) and X-ray Absorption Spectroscopy (XAS) provide a straightforward evidence of processes setting bistability. XAS spectra of the

Co $L_{2,3}$ thresholds are presented in **figure 4a** and do not reveal significant differences between the HRS and LRS. Both spectra are characteristic of predominantly metallic cobalt and lack pronounced satellite features that would indicate substantial cluster formation [32] or complete oxidation [33], although a weak shoulder is present on the high-energy side of both peaks that suggests the formation of a thin oxide layer, in agreement with the EELS data (SI2).

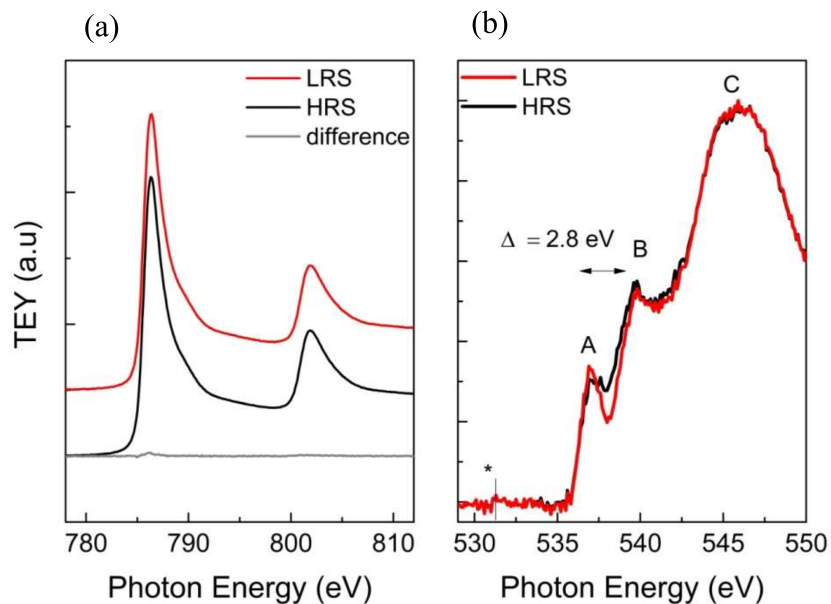

Figure 4(a) X-ray absorption spectra measured across the Co L absorption edge for LRS and HRS. Prior comparison, spectra were normalized by subtraction of a two step-like function with relative height of 2:1 [34]and overall scaling[32] (b) X-ray absorption spectra measured across the O K absorption edge for the HRS and LRS. Asterisk indicates the satellite peak for AlO_x contribution(see SI3); A, B, C are described in the text.

The interpretation of O K-edge spectra, shown in **figure 4b**, is more complicated because contributions arise from both AlO_x and Gaq_3 layers but an important result is that there are clear changes between the HRS and LRS. The spectra are dominated by a broad peak centered at E=546 eV (labeled 'C') and there are two satellites, at E= 539.8 eV ('B') and E= 537 eV ('A'). Previous studies of amorphous AlO_x layers [35] and Gaq_3 [36] allow feature A to be attributed to AlO_x (see SI3). Recent research [37] on AlO_x based RS devices uses the sharpness of this satellite peak as an indicator of the presence of oxygen vacancies, which in the films here could provide a migration pathway for oxygen through the barrier during switching. Indeed, it has been noted

elsewhere that AlO_x tunnel layers formed by the oxidation of aluminum thin films incorporate O_2^- ions that are weakly bound to the positively charged oxygen vacancies but are able to drift into and out of the barrier layer under electrical bias [38]. In this framework, the LRS, set after the application of a positive bias to the LSMO layer, would rely on the migration of negative charges (O_2^- included) towards the LSMO layer, leaving defective AlO_x. Oxygen represents a source of doping in our samples because the preparation of the tunnel barrier included O_2 exposure, in addition to brief exposure to the atmosphere before characterization[39].

To study in more detail the role of the AlO_x layer in RS, we analysed the Al chemical state directly by photoemission spectroscopy, as this allows direct isolation of the contribution of AlO_x alone. The HAXPES Al1s spectra shown in **figure 5a** are typically described by three components [18c]: a main peak corresponding to the AlO_x contribution [40] with two satellites at ΔE_1= +1.7 eV and ΔE_2= -2.5 eV. The lower binding energy contribution is associated with the metallic Al (Al-Al) while the broader contribution could be related to the higher oxidation states for Al, as for example Al_2O_3[40]. The HRS and LRS spectra indicate a subtle shift, relative to the IRS, of the main Al1s component only, which shifts by + (-) 0.1 eV for the H(L)RS, with a slightly broader lineshape (Γ=1.8). An Al1s core level shift to higher (lower) binding energy indicates a higher (lower) oxidation state [41], indicating that in the HRS the Al experiences increased oxygenation and a slightly more inhomogeneous chemical environment. The increase of oxygenation in HRS is confirmed by the relative percentage of the peak associated to the AlO_x with respect to the total area that is 78% while in LRS is 74%. (See SI4)

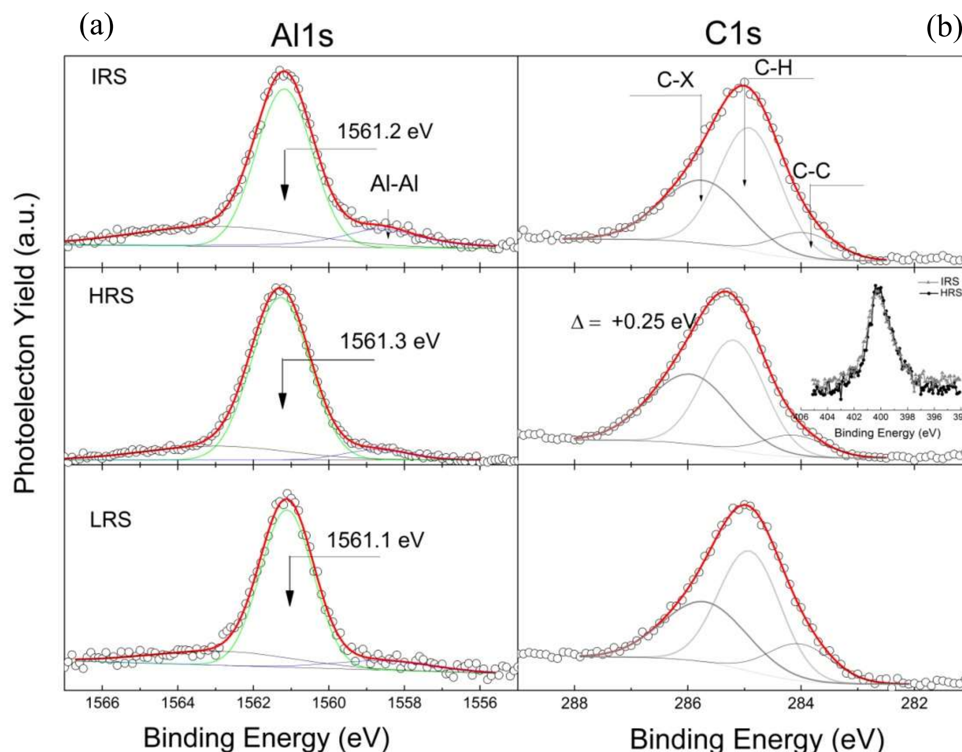

Figure 5 (a) Normalized HAXPES Al 1s spectra (open circles) for the IRS (top), HRS(intermediate) and LRS(bottom). Green and grey lines represent the three components and red lines the curve fit. (b) Normalized HAXPES C1s spectra (open circles) for IRS, HRS and LRS. Lines represent the three components and red lines the curve fit. Inset: HAXPES N1s spectra for IRS and HRS

Both O K-edge and Al1s analysis indicate a difference in the Al oxidation state between the LRS and HRS. We propose that the HRS, set by the application of a negative bias to the LSMO contact, is obtained by trapping of O_2^- in the AlO_X layer while the LRS, set by the application of positive bias to the LSMO contact, is obtained after migration of O_2^- away from the AlO_x. In the HRS, oxygen migration is not associated with any evident change in the Co layer (as observed in HAXPES), indicating that the AlO_x tunnel barrier is the principal oxygen trapping layer.

We turn now to the organic molecule. It is well established from theoretical calculations [42] that in metal quinoline complexes the highest occupied molecular orbital (HOMO) is located on the phenoxideside of the quinolinol ligands, whereas the lowest unoccupied molecular orbital

(LUMO) is found on the pyridyl side; the central metal ion (Ga) contributes negligibly to the density of states (DOS). Thus, it may be expected that any possible variations to the electronic configuration of the molecule during RS are most likely to produce a sizeable effect on the N1s or C1s HAXPES spectra. The C1s core levels HAXPES spectra for IRS, HRS and LRS are shown in **figure 5b**. They results from three main components corresponding to three bonding environments for carbon in the structure of the 8-quinolinol ligand (C–C bonds, C–H bonds, and C–X bonds where X stands for oxygen or nitrogen) and it is consistent with previous investigations [18c] of similar samples. During the fitting process, the area ratio for the C–C, C–H, and C–X components was kept 1:3:5, in agreement with their ratios in the complex. The binding energies of all three components do not change between the IRS and the LRS but in the HRS increase by 0.25 eV, which is generally a signature of an oxidation process (i.e. removal of electronic charge). Nevertheless, it is worth noting that a shift of C1s binding energy concurrent with a broadening of the N1s peak during deposition of Ca onto Alq3 has previously been attributed to charge donation and ligand dissociation [43]. In our case we did not observe any change in the N1s peak between the IRS and HRS (inset to Figure 5), excluding such effects. We therefore interpret the increase in C1s binding energy as a consequence of ionization of the molecule to form an Alq3 cation. This charge removal is reversible, since the HRS and LRS were cycled many times without changing their spectroscopic signatures. This picture is supported by an analysis of the XAS C-K-edge spectra shown in **figure 6**. XAS spectra relates to unoccupied states (in the presence of a core hole), as they reflect dipole-allowed transitions to empty molecular orbitals. HRS spectra are narrower than the corresponding LRS spectra, indicating an overall difference in the lower lying empty states. Figure 6a shows the calculated C K-edge spectra for the Gaq_3 molecule in its neutral form and after the removal of an electronic charge (Gaq_3 cation). Calculated spectra are in agreement with previous investigations [42a, 44] of bulk metal quinoline and feature more structured contributions with respect to experimental data, indicating that extrinsic broadening due to complex molecular

configuration is expected to dominate in devices. By a qualitative comparison of the measured and calculated spectra in neutral and positively charged states, the narrower experimental lineshape of the broad feature centered at 289 eV in HRS indicates a partial presence of a Gaq_3 cations.

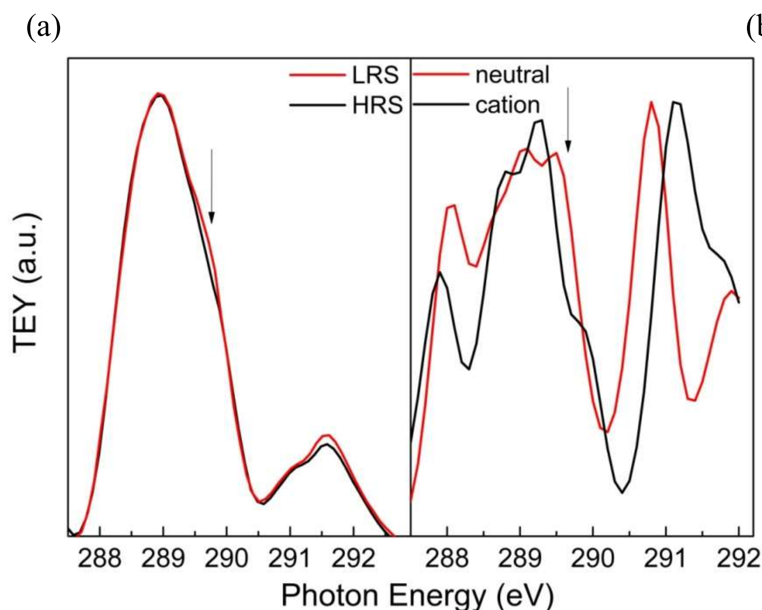

Figure 6 (a) X-ray absorption spectra measured across the C K absorption edge. (b)Calculated C K edge absorption spectra for neutral Gaq_3 molecule and for Gaq_3 cation obtained by a removal of an electronic charge.

Considering the Oxygen drift in and out the barrier, the reversible generation of positively charged states in Gaq_3 is then interpreted as a results of the formation of a charge-transfer complex involving the organic molecule and molecular oxygen [45]. A partial redistribution of the electronic charge within the complex yields then a negatively charged oxygen molecule and a hole on the quinoline ligand [46].

The positive charging of the organic molecules, modifying their electronic structure[47], results in a higher localization of electrons in the HOMO with respect to the neutral and negatively charged quinoline molecule. This localization of the HOMO would be unfavorable for electron hopping to a neighboring molecule and thus unfavorable for electron transport, as expected for HRS[47a]. We stress that XAS and HAXPES spectroscopic investigations average all over the

sample probing volume and thus changes of the electronic configuration of organic layer are not restricted to local conduction paths as expected in filamentary conduction process but involves all the organic molecules down to few nanometer from the interface with the AlO_x layer.

A schematic of the underlying physical processes during RS is presented in **figure 7**. The HRS is set by the application of a negative voltage to the LSMO: negative charges, including free electrons and O_2^- drift towards the Co top electrode. AlO_x then gets oxidized and acts as a trap, blocking the O_2^- ions and preventing interaction with Co. The oxygen drift is accompanied by a positive charging of the organic molecules, modifying the Gaq_3 electronic configuration[47a]: charges are generally more localized inside the individual quinoline unit inhibiting the electron transport and causing a subsequent increase of overall resistivity. In switching to the LRS by the application of a positive voltage to LSMO, oxygen migrates towards the LSMO layer to leave a defective AlO_x barrier and restore the neutrality of the Gaq_3 molecule.

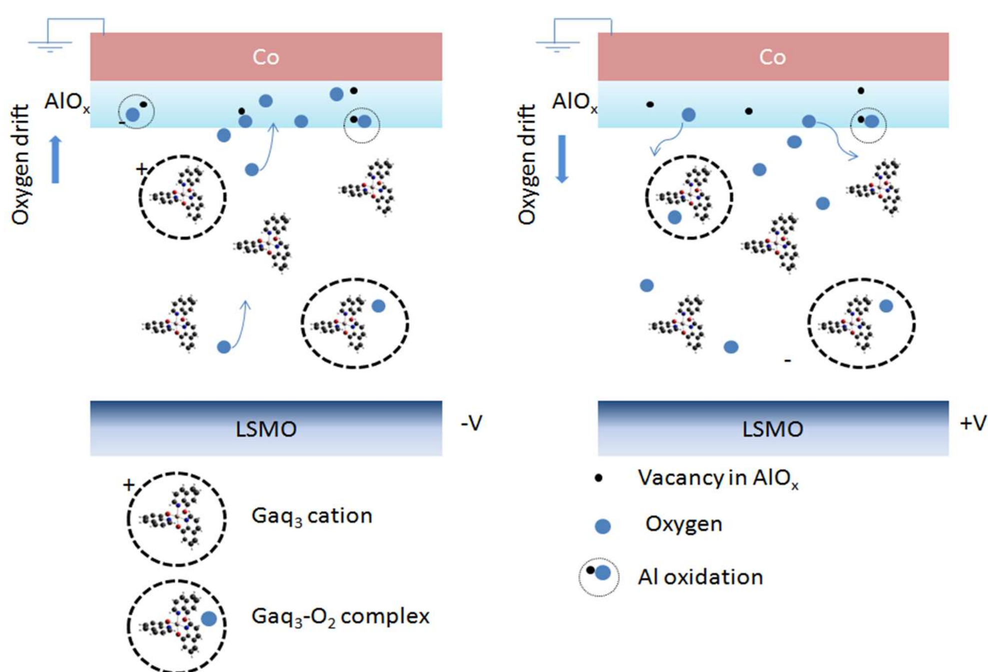

Figure 7 Schematic representation of RS: HRS (left) and LRS (right). HRS is set by the application of a negative voltage to the LSMO: negative charges, including free electrons and O_2^- drift towards the Co top electrode. The AlO_x is oxidized and acts as trap, blocking the O_2^- ions and preventing interaction with Co. The oxygen drift is accompanied by a positive charging

of the organic molecules. Switching to the LRS, oxygen migrates towards the LSMO layer to leave a defective AlO_x barrier and restore the neutrality of the Gaq_3 molecule.

Once established that resistive switching is associated to oxygen migration across the organic layer and to a reversible formation of Gaq_3 cations, we discuss the correlation with MR.

An important issue to take into account is the voltage regime at which bistability and MR are found. While bistability is set by applying few V to our device, MR is detectable only at extremely small voltages (≤ 0.1 V) which are much lower than interfacial electronic barriers for the charge injection into HOMO or LUMO level[48]. Such peculiar MR voltage dependence together with the absence of Hanle effect [12] expected in case of HOMO-LUMO transport, pushed several authors [7b, 11b] to propose a qualitatively different picture to describe spin transport in the OSVs based on the presence of intragap localized levels. Recently the impurity band model [13a] was proposed to explain MR in regimes far from the direct tunneling from electrodes, but its experimental validation has yet to be accomplished.

In our case, the MR intensity depends on the specific resistive state in which the device is put: on the basis of results above, MR is absent when a more efficient insulating AlO_x barrier is set and Gaq_3 cations are formed, while MR has its maximum value in case of defective AlO_x barrier and after oxygen ions migration into the organic layer and the formation of complexes.

We expect then that AlO_x defective barrier [49] will generate a number of localized states able to promote the spin injection from the Cobalt electrode into the organic layer where the spin transport takes place in presence of Oxygen ions acting as dopant (or impurity), via the formation of complexes with Gaq_3. Our data are consistent with the formation of intragap impurity levels as proposed theoretically by Yu[13a] to describe spin and charge transport in spin valves. Same model includes a quite inhomogeneous doping density distribution compatible with the expected formation of conduction paths or filaments and the establishment of a local impurity band.

The decrease of MR corresponds to more efficient insulating AlOx barrier [49], that limits the tunneling into the organic layer, and to a lower density of impurities that in association with electronic localization of Gaq_3 cations increases the residence time of spin/charges, which have the effect of enhancing spin dephasing processes[50].

Oxygen as dopant in organics can in principle originate from intrinsic doping during deposition. Interestingly, among devices presenting reproducible MR in literature most of them have the LSMO oxide[8, 24, 51] as electrode or include the presence of oxide tunnel tunnel barrier [22, 52] indicating the oxide layers as most plausible sources of oxygens in such devices. Recently Grünewald *et al.*[3c], discussing similar devices, advanced a model ascribing both the resistive switching and magnetic characteristics uniquely to oxygen variations in the LSMO electrode. Our set of data do not access the interfacial LSMO layer in reason of the limited electron escape depth for Hard X-Ray photoemission, providing little access to the deep buried interface with LSMO layer. Nevertheless, our data provide a complementary interpretation of the mechanism, indicating significant modifications of the stoichiometry of the aluminum oxide barrier and substantial oxygen diffusion inside the organic layer, both factors controlling the device resistance.[53]

3. Conclusions

In summary, we have demonstrated that resistive switching effect in LSMO/Gaq_3/AlOx/Co devices is driven by the oxygen migration across the structure: both AlOx tunnel barrier and Gaq_3 layer reversibly change the oxygen concentrations while switching between the high and the low resistive states. The reversible shift of the C peak by the programing voltage indicates that the oxygenated organic layer is a key element for establishing both the bistability and magnetoresistance behaviors, although at this stage it is difficult to separate quantitatively the roles of Gaq_3 and AlO_x layers. These findings shed important light on the still unidentified

mechanism of magnetoresistance in this class of devices and represent the first experimental evidence in support of the recently proposed impurity band model.

4. Experimental section

Samples were prepared *ex-situ* using Channel Spark ablation deposition for LSMO [54], thermal evaporation for Gaq_3 and Al and electron beam evaporation for Co layer. AlO_x was obtained by exposing the Al layer to a partial pressure of O_2.

Transmission electron microscopy (TEM) was employed for structural characterization, using a probe-corrected JEOL ARM200cF instrument that was operated at 200 kV and is equipped with a cold field emission electron gun and a Gatan Quantum electron energy loss spectrometer. Cross-sectional samples were prepared using standard 'lift-out' procedures on an FEI Nova Nanolab Focused Ion Beam instrument and were typically polished to ~100 nm thickness: further thinning tended to damage the delicate organic layer. Electron energy loss spectroscopy (EELS) data were acquired using the spectrum imaging [55] and dual EELS [56] methodologies within Gatan's Digital Micrograph software, which was also used for data processing.

Full magnetoresistive characterization was carried out in a 4-point cross bar configuration by using a Keithley 236 SMU in the temperature range 100-300K with a maximum applied field of $\mu H=0.3$ T. The LSMO electrode was biased while the Co was kept at ground. Impedance spectra were recorded with an Agilent E4980A LCR-Meter in the 20-100k Hz range in order to distinguish between capacitive and ohmic behavior.

Chemical investigation by Hard X-ray Photoelectron Spectroscopy (HAXPES) and X-ray Absorption Spectroscopy (XAS) was performed at room temperature on a sample holder that allows current voltage (I-V) characterization in a 2 point configuration directly within the analysis chamber. The large depth sensitivity achievable by HAXPES (~ 15 nm) and by XAS (~ 7 nm) allowed us to investigate deep regions within a working device and to study the effects of the resistive switching on the top electrode, the underlying organic layer and the interfaces

with the barrier layer. Devices presented a retention time [5a] that greatly surpassed the HAXPES and XAS measurement timescale, ensuring that the observed spectroscopic signatures are unambiguously associated with specific resistance states.

XAS measurements were performed across the Co $L_{2,3}$, O-K and C-K absorption edges at the BEAR beamline (Elettra-Trieste)[57]. Spectra are acquired in total electron yield mode, by measuring the sample drain current, and they are normalized to the beam flux by using a clean gold sample as reference. HAXPES spectra were collected from the Al1s, C1s, Ga1s, N1s core levels at the GALAXIES beamline (Synchrotron SOLEIL, Paris) [58] using an excitation energy of 7.2KeV. Fits were carried out by XPSpeak software .To eliminate the prospect of oxidation and contamination of the air-exposed side of the Co electrode, all the samples were mildly Ar^+-sputtered (E=500 eV for 30min) in the preparation chamber before spectroscopic investigations. Surface cleanliness was checked by monitoring the surface-sensitive C and O XPS signals. To minimize sample damage under prolonged x-ray exposure, the beam footprint was moved frequently across the device

The XAS simulations were performed on the free Gaq_3 molecule using the transition-potential method using the StoBe DFT simulation code. [59]An IGLO-III basis set was used on each excitation center, while effective core potentials were used for the remaining C atoms. The calculated dipole-excitation spectra were Gaussian convoluted with an energy-dependent broadening and aligned to the experimental curves.

Acknowledgements

This work is funded through the European Union Seventh Framework Programme (FP7/2007-2013) under grant agreement GA No. 263104 and COST action 15128. We thank SOLEIL and ELETTRA synchrotrons for provision of synchrotron radiation facilities at beamline GALAXIES (proposal number 20130329) and beamline BEAR (proposal number 20135188) respectively.

Received: ((will be filled in by the editorial staff))
Revised: ((will be filled in by the editorial staff))
Published online: ((will be filled in by the editorial staff))

References

[1] J. C. Scott, L. D. Bozano, *Advanced Materials* **2007**, 19, 1452.
[2] C.-H. Tu, Y.-S. Lai, K. Dim-Lee, *Electron Device Letters, IEEE* **2006**, 27, 354.
[3] a) L. E. Hueso, I. Bergenti, A. Riminucci, Y. Q. Zhan, V. Dediu, *Advanced Materials* **2007**, 19, 2639; b) M. Prezioso, A. Riminucci, I. Bergenti, P. Graziosi, D. Brunel, V. A. Dediu, *Advanced Materials* **2011**, 23, 1371; c) M. Grünewald, N. Homonnay, J. Kleinlein, G. Schmidt, *Physical Review B* **2014**, 90, 205208.
[4] V. Dediu, L. E. Hueso, I. Bergenti, A. Riminucci, F. Borgatti, P. Graziosi, C. Newby, F. Casoli, M. P. De Jong, C. Taliani, Y. Zhan, *Physical Review B* **2008**, 78, 115203.
[5] a) M. Prezioso, A. Riminucci, P. Graziosi, I. Bergenti, R. Rakshit, R. Cecchini, A. Vianelli, F. Borgatti, N. Haag, M. Willis, A. J. Drew, W. P. Gillin, V. A. Dediu, *Advanced Materials* **2013**, 25, 534; b) V. K. Sangwan, D. Jariwala, I. S. Kim, K.-S. Chen, T. J. Marks, L. J. Lauhon, M. C. Hersam, *Nat Nano* **2015**, 10, 403.
[6] a) P. Krzysteczko, J. Münchenberger, M. Schäfers, G. Reiss, A. Thomas, *Advanced Materials* **2012**, 24, 762; b) K. Zhang, Y.-l. Cao, Y.-w. Fang, Q. Li, J. Zhang, C.-g. Duan, S.-s. Yan, Y.-f. Tian, R. Huang, R.-k. Zheng, S.-s. Kang, Y.-x. Chen, G.-l. Liu, L.-m. Mei, *Nanoscale* **2015**, 7, 6334.
[7] a) D. Sun, L. Yin, C. Sun, H. Guo, Z. Gai, X. G. Zhang, T. Z. Ward, Z. Cheng, J. Shen, *Physical Review Letters* **2010**, 104, 236602; b) C. Barraud, P. Seneor, R. Mattana, S. Fusil, K. Bouzehouane, C. Deranlot, P. Graziosi, L. Hueso, I. Bergenti, V. Dediu, F. Petroff, A. Fert, *Nat Phys* **2010**, 6, 615.
[8] Z. H. Xiong, D. Wu, Z. Valy Vardeny, J. Shi, *Nature* **2004**, 427, 821.
[9] V. A. Dediu, A. Riminucci, *Nat Nano* **2013**, 8, 885.
[10] a) P. P. Ruden, D. L. Smith, *Journal of Applied Physics* **2004**, 95, 4898; b) A. Goswami, M. Yunus, P. P. Ruden, D. L. Smith, *Journal of Applied Physics* **2012**, 111, 034505.
[11] a) M. Gobbi, F. Golmar, R. Llopis, F. Casanova, L. E. Hueso, *Advanced Materials* **2011**, 23, 1609; b) T. L. A. Tran, T. Q. Le, J. G. M. Sanderink, W. G. van der Wiel, M. P. de Jong, *Advanced Functional Materials* **2012**, 22, 1180.
[12] A. Riminucci, M. Prezioso, C. Pernechele, P. Graziosi, I. Bergenti, R. Cecchini, M. Calbucci, M. Solzi, V. A. Dediu, *Applied Physics Letters* **2013**, 102.
[13] a) Z. G. Yu, *Nat Commun* **2014**, 5; b) A. V. Shumilin, V. V. Kabanov, V. A. Dediu, *New Journal of Physics* **2015**, 17.
[14] P.-T. Lee, T.-Y. Chang, S.-Y. Chen, *Organic Electronics* **2008**, 9, 916.
[15] C. W. Chu, J. Ouyang, J. H. Tseng, Y. Yang, *Advanced Materials* **2005**, 17, 1440.
[16] a) M. Cölle, M. Büchel, D. M. de Leeuw, *Organic Electronics* **2006**, 7, 305; b) Y. Busby, S. Nau, S. Sax, E. J. W. List-Kratochvil, J. Novak, R. Banerjee, F. Schreiber, J.-J. Pireaux, *Journal of Applied Physics* **2015**, 118, 075501.
[17] B. Li, J.-W. Yoo, C.-Y. Kao, H. W. Jang, C.-B. Eom, A. J. Epstein, *Organic Electronics* **2010**, 11, 1149.
[18] a) Y. Q. Zhan, X. J. Liu, E. Carlegrim, F. H. Li, I. Bergenti, P. Graziosi, V. Dediu, M. Fahlman, *Applied Physics Letters* **2009**, 94, 053301; b) A. A. Sidorenko, C. Pernechele, P. Lupo, M. Ghidini, M. Solzi, R. De Renzi, I. Bergenti, P. Graziosi, V. Dediu, L. Hueso, A. T. Hindmarch, *Applied Physics Letters* **2010**, 97, 162509; c) F. Borgatti, I. Bergenti, F. Bona, V. Dediu, A. Fondacaro, S. Huotari, G. Monaco, D. A. MacLaren, J. N. Chapman, G. Panaccione, *Applied Physics Letters* **2010**, 96, 043306.

[19] A. Droghetti, S. Steil, N. Großmann, N. Haag, H. Zhang, M. Willis, W. P. Gillin, A. J. Drew, M. Aeschlimann, S. Sanvito, M. Cinchetti, *Physical Review B* **2014**, 89, 094412.
[20] L. D. Bozano, B. W. Kean, V. R. Deline, J. R. Salem, J. C. Scott, *Applied Physics Letters* **2004**, 84, 607.
[21] R. Waser, M. Aono, *Nat Mater* **2007**, 6, 833.
[22] J. J. H. M. Schoonus, P. G. E. Lumens, W. Wagemans, J. T. Kohlhepp, P. A. Bobbert, H. J. M. Swagten, B. Koopmans, *Physical Review Letters* **2009**, 103, 146601.
[23] R. Lin, F. Wang, J. Rybicki, M. Wohlgenannt, K. A. Hutchinson, *Physical Review B* **2010**, 81, 195214.
[24] S. W. Jiang, D. J. Shu, L. Lin, Y. J. Shi, J. Shi, H. F. Ding, J. Du, M. Wang, D. Wu, *New Journal of Physics* **2014**, 16.
[25] S. Berleb, W. Brütting, *Physical Review Letters* **2002**, 89, 286601.
[26] P. Sebastian, F. Lindner, K. Walzer, B. Lüssem, K. Leo, *Journal of Applied Physics* **2011**, 110, 084508.
[27] S. Nau, S. Sax, E. J. W. List-Kratochvil, *Advanced Materials* **2014**, 26, 2508.
[28] B. Cho, S. Song, Y. Ji, T.-W. Kim, T. Lee, *Advanced Functional Materials* **2011**, 21, 2806.
[29] L. F. Pender, R. J. Fleming, *Journal of Applied Physics* **1975**, 46, 3426.
[30] S. Gao, C. Song, C. Chen, F. Zeng, F. Pan, *The Journal of Physical Chemistry C* **2012**, 116, 17955.
[31] Y. Xu, D. Ephron, M. R. Beasley, *Physical Review B* **1995**, 52, 2843.
[32] P.-Y. Cheng, M.-R. Chiang, Y.-L. Chan, Y.-J. Hsu, P.-C. Wang, D. H. Wei, *Applied Physics Letters* **2014**, 104, 043303.
[33] N. D. Telling, G. van der Laan, S. Ladak, R. J. Hicken, E. Arenholz, *Journal of Applied Physics* **2006**, 99, 08E505.
[34] Z. L. Wang, J. Bentley, N. D. Evans, *Micron* **2000**, 31, 355.
[35] C. Århammar, A. Pietzsch, N. Bock, E. Holmström, C. M. Araujo, J. Gråsjö, S. Zhao, S. Green, T. Peery, F. Hennies, S. Amerioun, A. Föhlisch, J. Schlappa, T. Schmitt, V. N. Strocov, G. A. Niklasson, D. C. Wallace, J.-E. Rubensson, B. Johansson, R. Ahuja, *Proceedings of the National Academy of Sciences* **2011**, 108, 6355.
[36] a) T. Yokoyama, H. Ishii, N. Matsuie, K. Kanai, E. Ito, A. Fujimori, T. Araki, Y. Ouchi, K. Seki, *Synthetic Metals* **2005**, 152, 277; b) S. Fang, Z. Pang, Y. Du, L. Zheng, X. Zhang, F. Wang, H. Yuan, S. Han, *Journal of Applied Physics* **2012**, 112, 113519.
[37] S. Nigo, M. Kubota, Y. Harada, T. Hirayama, S. Kato, H. Kitazawa, G. Kido, *Journal of Applied Physics* **2012**, 112, 033711.
[38] E. Tan, P. G. Mather, A. C. Perrella, J. C. Read, R. A. Buhrman, *Physical Review B* **2005**, 71, 161401.
[39] J. Laubender, L. Chkoda, M. Sokolowski, E. Umbach, *Synthetic Metals* **2000**, 111–112, 373.
[40] P. Risterucci, O. Renault, C. Zborowski, D. Bertrand, A. Torres, J. P. Rueff, D. Ceolin, G. Grenet, S. Tougaard, *Applied Surface Science* **2017**, 402, 78.
[41] V. Kottler, M. F. Gillies, A. E. T. Kuiper, *Journal of Applied Physics* **2001**, 89, 3301.
[42] a) A. Curioni, W. Andreoni, R. Treusch, F. J. Himpsel, E. Haskal, P. Seidler, C. Heske, S. Kakar, T. van Buuren, L. J. Terminello, *Applied Physics Letters* **1998**, 72, 1575; b) F. Bisti, A. Stroppa, M. Donarelli, S. Picozzi, L. Ottaviano, *Physical Review B* **2011**, 84, 195112.
[43] S. C. Kim, J. W. Kim, J. Lee, Y. Park, *Journal of the Korean Physical Society* **2008**, 53, 812.

[44] A. DeMasi, L. F. J. Piper, Y. Zhang, I. Reid, S. Wang, K. E. Smith, J. E. Downes, N. Peltekis, C. McGuinness, A. Matsuura, *The Journal of Chemical Physics* **2008**, 129, 224705.
[45] a) M. S. A. Abdou, F. P. Orfino, Y. Son, S. Holdcroft, *Journal of the American Chemical Society* **1997**, 119, 4518; b) R. Di Pietro, D. Fazzi, T. B. Kehoe, H. Sirringhaus, *Journal of the American Chemical Society* **2012**, 134, 14877.
[46] A. Y. Karmilov, N. A. Sysoeva, A. L. Buchachenko, *Journal of Structural Chemistry* **1978**, 18, 649.
[47] a) R. Q. Zhang, C. S. Lee, S. T. Lee, *Chemical Physics Letters* **2000**, 326, 413; b) A. Curioni, M. Boero, W. Andreoni, *Chemical Physics Letters* **1998**, 294, 263.
[48] Y. Q. Zhan, M. P. de Jong, F. H. Li, V. Dediu, M. Fahlman, W. R. Salaneck, *Physical Review B* **2008**, 78, 045208.
[49] X. Sun, M. Gobbi, A. Bedoya-Pinto, O. Txoperena, F. Golmar, R. Llopis, A. Chuvilin, F. Casanova, L. E. Hueso, *Nature Communications* **2013**, 4, 2794.
[50] L. E. Hueso, J. M. Pruneda, V. Ferrari, G. Burnell, J. P. Valdes-Herrera, B. D. Simons, P. B. Littlewood, E. Artacho, A. Fert, N. D. Mathur, *Nature* **2007**, 445, 410.
[51] R. Göckeritz, N. Homonnay, A. Müller, B. Fuhrmann, G. Schmidt, *AIP Advances* **2016**, 6, 045003.
[52] a) T. S. Santos, J. S. Lee, P. Migdal, I. C. Lekshmi, B. Satpati, J. S. Moodera, *Physical Review Letters* **2007**, 98, 016601; b) X. Zhang, S. Mizukami, Q. Ma, T. Kubota, M. Oogane, H. Naganuma, Y. Ando, T. Miyazaki, *Journal of Applied Physics* **2014**, 115, 172608; c) M. Galbiati, S. Tatay, S. Delprat, H. L. Khanh, B. Servet, C. Deranlot, S. Collin, P. Seneor, R. Mattana, F. Petroff, *Applied Physics Letters* **2015**, 106, 082408.
[53] K. J. O'Shea, D. A. MacLaren, D. McGrouther, D. Schwarzbach, M. Jungbauer, S. Hühn, V. Moshnyaga, R. L. Stamps, *Nano Letters* **2015**, 15, 5868.
[54] P. Graziosi, M. Prezioso, A. Gambardella, C. Kitts, R. K. Rakshit, A. Riminucci, I. Bergenti, F. Borgatti, C. Pernechele, M. Solzi, D. Pullini, D. Busquets-Mataix, V. A. Dediu, *Thin Solid Films* **2013**, 534, 83.
[55] J. A. Hunt, D. B. Williams, *Ultramicroscopy* **1991**, 38, 47.
[56] J. Scott, P. J. Thomas, M. MacKenzie, S. McFadzean, J. Wilbrink, A. J. Craven, W. A. P. Nicholson, *Ultramicroscopy* **2008**, 108, 1586.
[57] S. Nannarone, F. Borgatti, A. DeLuisa, B. P. Doyle, G. C. Gazzadi, A. Giglia, P. Finetti, N. Mahne, L. Pasquali, M. Pedio, G. Selvaggi, G. Naletto, M. G. Pelizzo, G. Tondello, *AIP Conference Proceedings* **2004**, 705, 450.
[58] J.-P. Rueff, J. M. Ablett, D. Ceolin, D. Prieur, T. Moreno, V. Baledent, B. Lassalle-Kaiser, J. E. Rault, M. Simon, A. Shukla, *Journal of Synchrotron Radiation* **2015**, 22, 175.
[59] a) K. Hermann, L. G. M. Pettersson, M. E. Casida, C. Daul, A. Goursot, A. Koester, E. Proynov, A. St-Amant, D. R. Salahub, V. Carravetta, 2007; b) L. Triguero, L. G. M. Pettersson, H. Ågren, *Physical Review B* **1998**, 58, 8097.

Copyright WILEY-VCH Verlag GmbH & Co. KGaA, 69469 Weinheim, Germany, 2016.